A scalable filtration method for high throughput screening based on cell deformability

Journal:	*Lab on a Chip*
Manuscript ID	LC-ART-08-2018-000922.R1
Article Type:	Paper
Date Submitted by the Author:	11-Nov-2018
Complete List of Authors:	Gill, Navjot; University of California Los Angeles, Integrative Biology and Physiology Ly, Chau; University of California, Los Angeles, USA , Department of Bioengineering Nyberg, Kendra; University of California Los Angeles, Integrative Biology and Physiology Lee, Linus; University of California, Los Angeles, USA , Department of Integrative Biology and Physiology Qi, Dongping; UCLA, Integrative biology and Physiology; Cytolumina Technologies Corp. Tofig, Bobby; University of California, Los Angeles, USA, Molecular Screening Shared Resource California NanoSystems Institute Reis-Sobreiro, Mariana; Cedars-Sinai Medical Center, Department of Surgery and Biomedical Sciences Dorigo, Oliver; Stanford University, OB GYN Rao, Jianyu; University of California, Los Angeles, Wiedemeyer, Ruprecht ; Cedars-Sinai Medical Center, Samuel Oschin Comprehensive Cancer Institute Karlan, Beth; Cedars-Sinai Medical Center, Samuel Oschin Comprehensive Cancer Institute Lawrenson, Kate; Cedars-Sinai Medical Center, Samuel Oschin Comprehensive Cancer Institute Freeman, Michael; Cedars-Sinai Medical Center, Department of Surgery and Biomedical Sciences Damoiseaux, Robert; University Of California, Los Angeles, Molecular Screening Shared Resources Rowat, Amy; University of California, Los Angeles, Integrative Biology & Physiology

A scalable filtration method for high throughput screening based on cell deformability

Navjot Kaur Gill, Chau Ly, Kendra D. Nyberg, Linus Lee, Dongping Qi, Bobby Tofig,
Mariana Reis-Sobreiro, Oliver Dorigo, JianYu Rao, Ruprecht Wiedemeyer, Beth Karlan,
Kate Lawrenson, Michael R Freeman, Robert Damoiseaux, Amy C. Rowat

Abstract

Cell deformability is a label-free biomarker of cell state in physiological and disease contexts ranging from stem cell differentiation to cancer progression. Harnessing deformability as a phenotype for screening applications requires a method that can simultaneously measure the deformability of hundreds of cell samples and can interface with existing high throughput facilities. Here we present a scalable cell filtration device, which relies on the pressure-driven deformation of cells through a series of pillars that are separated by micron-scale gaps on the timescale of seconds: less deformable cells occlude the gaps more readily than more deformable cells, resulting in decreased filtrate volume which is measured using a plate reader. The key innovation in this method is that we design customized arrays of individual filtration devices in a standard 96-well format using soft lithography, which enables multiwell input samples and filtrate outputs to be processed with higher throughput using automated pipette arrays and plate readers. To validate high throughput filtration to detect changes in cell deformability, we show the differential filtration of human ovarian cancer cells that have acquired cisplatin-resistance, which is corroborated with cell stiffness measurements using quantitative deformability cytometry. We also demonstrate differences in the filtration of human cancer cell lines, including ovarian cancer cells that overexpress transcription factors (Snail, Slug), which are implicated in epithelial-to-mesenchymal transition; breast cancer cells (malignant versus benign); and prostate cancer cells that exhibit a malignant phenotype. We additionally show how the filtration of ovarian cancer cells is affected by treatment with drugs known to perturb the cytoskeleton and the nucleus. Our results across multiple cancer cell types with both genetic and pharmacologic manipulations demonstrate the potential of this scalable filtration device to screen cells based on their deformability.

Key words: Cell mechanical properties, cell mechanotype, microfluidics, cancer cells

Introduction

High throughput (HT) assays enable screening of cells against thousands of compounds in chemical libraries[1-4]. Typical screens are based on molecular readouts such as gene or protein expression[5-7], or cellular behaviors such as proliferation[8,9], apoptosis[10,11], or invasion[12,13]. Screens based on such molecular and cellular metrics have enabled the identification of drugs with clinical efficacy[14,15]. For example, the commonly used anti-cancer agent, paclitaxel, was discovered in a high throughput screen based on its ability to stop cell proliferation[16]. While the development of treatment strategies using existing drugs has led to significant progress in improving patient survival and disease outcome[17-21], the majority of deaths occur due to metastasis and recurrence[22-24]. Thus, there is an urgent need to identify novel therapeutic agents. A promising strategy to discover new compounds is by assaying alternative cellular phenotypes that are implicated in cancer progression and metastasis[25], such as cellular metabolism[26], adhesion[13,27], or deformability[28-31].

Screening for chemotherapeutics based on the intrinsic deformability of cells has exciting potential. A variety of clinically used chemotherapy agents, such as daunorubicin and paclitaxel, increase the stiffness of cancer cells[28,32-34]; this induced stiffening may result from cell death[32] and/or stabilization of microtubules to cause cell cycle arrest and stop proliferation[28,35]. Other desirable targets for cancer therapies include Rho GTPase[36] and Rho-associated protein kinase[37], which regulate actin structure, dynamics, and cell motility; these are also major regulators of cellular deformability[36,38,39]. Since the deformability of cancer cells is associated with cellular invasion[29,40-42], compounds that make cancer cells stiffer may also decrease their invasion. Consistent with this idea, we previously found that ovarian cancer cells (OVCA433) with induced expression of transcription factors implicated in epithelial-to-mesenchymal transition [43] are more deformable than epithelial-like cells[28]; EMT is also accompanied by increased cell invasion[44]. Our previous work also shows that ovarian cancer cells with acquired resistance to the common chemotherapy agent cisplatin have mesenchymal-type features and are more deformable than cisplatin-sensitive cells[28]. Thus, identifying small molecules based on their ability to revert the deformability of cancer cells—especially mesenchymal-like, drug-resistant cells—to levels of less invasive and/or normal cells could provide a route to identify complementary compounds that inhibit cancer cell behaviors such as proliferation and motility.

While cancer cell deformability as a phenotype has potential for drug discovery, there are thousands of drugs in typical libraries for high throughput screening. However, existing mechanotyping methods rely on sequential measurements of individual cell samples. Methods to measure cell mechanical properties, such as atomic force microscopy or magnetic twisting cytometry, achieve measurements of elastic modulus through detailed force-deformation profiling on single cells, but have limited throughput[45-48]. Microfluidic-based methods enable rapid measurements of the deformability of single cell populations[49-51], but rely on customized image analysis of individual cells and samples sequentially, which is a computationally expensive bottleneck. Such methods are thus challenging to integrate into high throughput facilities that rely on treating and processing hundreds of samples in multiwell plates simultaneously. If a method to measure cell deformability could be integrated into existing high throughput sample handling platforms that use multiwell inputs and readouts, this would enable deformability to be used as a phenotype for drug discovery.

To enable simultaneous measurements of cell deformability, we recently developed the parallel microfiltration method[28,52]. Parallel microfiltration relies on the filtration of a cell suspension across a polycarbonate membrane with micron-scale pores; stiffer cells are more likely to occlude pores compared to more deformable cells. The concept of filtration for measuring cell deformability has been established for different red and white blood cell types[53-55], as well as cancer cells[28,41,42]. While we previously established proof-of-concept measurements of cell deformability using a prototype parallel microfiltration device, there are numerous challenges to scaling up this method. The prototype device requires measuring the retained sample volumes across the plate, which involves additional steps of liquid handling. Moreover, manual assembly is required to set up the device: commercially available polycarbonate membranes are manually placed in the prototype device, which is tightened to achieve a pressure-tight seal[28]. Such manual processing introduces user variation, and thus measurement variability. All of these challenges hinder the scale-up of parallel microfiltration for robust, HT assays.

Here we present a scalable high throughput filtration (HTF) method that enables multiple samples to be measured simultaneously. Inspired by strategies to scale-up microfluidic devices for HT applications[56-60], the core of HTF is a custom-fabricated array of 96 microfiltration devices; each device contains a series of pillars with well-defined micron-scale gaps from 6 to 14 μm that are smaller than the diameter of single cells. Cells are driven to passively deform through the gaps on the timescale of seconds to minutes in response to applied pressure. The ability of cells to deform through the gaps determines the fluidic resistance of a single device: a larger number of cells that occlude gaps results in a higher fluidic resistance, less flow through the filtration device, and thus a smaller filtrate volume. Importantly, the volume of collected filtrate can be rapidly measured in multiwell format using a plate reader, thereby enabling automation of cell filtration measurements. To characterize the HTF method and operational parameters, we measure the filtration of cisplatin-sensitive (OVCAR5 Cis-S) versus -resistant human ovarian cancer (OVCAR5 Cis-R) cells, which we independently confirm have distinct elastic moduli using quantitative deformability cytometry[61]. To validate the HTF method to distinguish cell samples, we screen human ovarian cancer (OVCA433 GFP, Snail and Slug) cells with induced EMT by overexpression of transcription factors (Snail, Slug), and treat these cells with a panel of cytoskeletal and nuclear perturbing drugs that modulate cell deformability. To demonstrate broader applicability of HTF for screening cells based on cell deformability, we filter malignant human breast cancer cells (MDA-MB-468, MDA-MB-231) versus non-tumorigenic breast epithelial (MCF10A) cells, and weakly metastatic prostate cancer (DU145) cells versus DU145 cells transformed with knock down of nuclear envelope protein, emerin (DU145 Emerin KD), which are highly metastatic. Taken together, our results demonstrate the potential of HTF as a scalable platform for screening based on cell deformability.

Methods

Cell culture: Human ovarian cancer (OVCA433), breast cancer (triple negative MDA-MB-468 and MDA-MB-231), and prostate cancer (DU145) cells are cultured in DMEM (+L-Glutamine, +Glucose, +Sodium Pyruvate) supplemented with 10% FBS, 1% Anti-anti (Gibco). For OVCA433 GFP (control), SNAI1-overexpressing cells (OVCA433 Snail), and SNAI2-overexpressing cells (OVCA433 Slug) (Qi et al., 2015) we use the same media with the addition of blasticidin S HCl (5 µg/ml, Corning Cellgro). To culture the cisplatin-sensitive and -resistant cells, OVCAR5 Cis-S/OVCAR5 Cis-R, we use Dulbecco's Modified Eagle Medium (DMEM) with 10% FBS, 1% Penicillin-Streptomycin, and 10 µM cisplatin (Sigma-Aldrich) for the resistant cells. To culture immortalized non-tumorigenic breast epithelial (MCF10A) cells, we use Mammary Epithelial Cell Growth Basal Medium (MEBM) (Lonza) supplemented with bovine pituitary extract (52 µg/mL), hydrocortisone (0.5 µg/mL), human EGF (10 ng/mL), and insulin (5 µg/mL) (MEGM Bullet Kit, Lonza) as well as 100 ng/mL cholera toxin (Sigma Aldrich). DU145 Emerin KD cells are cultured in DMEM with 10% FBS, 1% Penicillin-Streptomycin, and 2 µg/mL puromycin (Thermo Fisher Scientific). Prior to filtration measurements, cells are washed with 1x Phosphate-Buffered Saline (PBS, DNase-, RNase- & Protease- free, Mediatech, Manassas, USA), treated with trypsin, and resuspended in fresh medium to a density of 0.5 x 10^6 cells/mL. To minimize clusters of cells, cell suspensions are passed through a 35 µm cell strainer (BD Falcon) prior to each filtration measurement.

Drug treatments: Stock solutions of paclitaxel (451656, Corning Cellgro), cytochalasin-D (C8273, Sigma-Aldrich), colchicine (C9754, Sigma-Aldrich), paclitaxel (T7402, Sigma-Aldrich), blebbistatin (ab120425, Abcam), SB43154 (1614, Tocris), verteporfin (5305, Tocris), and trichostatin-A (1406, Tocris) are prepared according to manufacturer instructions. Cells are treated with 0.1 to 10 µM of drugs as indicated for 24 h prior to measurements.

Device fabrication: To fabricate the HTF microfluidic device array, two polydimethylsiloxane (PDMS, Sylgard 184 silicone elastomer, Dow Corning) layers are individually fabricated and then covalently bonded together. To produce the first layer that contains the 10 µm-height filtration devices, we spin coat SU-8 3005 photoresist (Microchem) at spin speed of 100 rpm to a thickness of 10 µm on a 6” silicon wafer (Silicon Valley microelectronics). The thickness of the photoresist is confirmed to be 9.7 ± 0.1 µm using a Dektak 150 Surface Profilometer (Veeco). A 10:1 w/w base to crosslinker ratio of PDMS is poured onto the master wafer, degassed using a desiccator vacuum for 20 minutes, and cured at 65 °C for 2 h. We use the same protocol to mold the second layer that contains outlets that are cast using a 96 x 250 µL array of pipette tips. The surfaces of the two layers to be bonded are then exposed to UV light in the presence of ozone[62] for 5 minutes using a UVO cleaner 42 (Jetlight). Outlets in the second PDMS layer are aligned with the inlet regions of the filtration devices in the first PDMS layer and pressed gently to bond. Filtration measurements are performed 24 h after bonding to ensure consistent surface properties across experiments[63].

HT-cell filtration: Cell suspension (350 µL) at 0.5 x 10^6 cells/mL or otherwise shown cell concentration is loaded into each well of the 96-well loading plate. We adapt plasmid filtration plate (HyperSep filter plate, Thermo Fisher) with filters removed as the loading plate. To measure cell number, we use an automated cell counter (TC20, BioRad); these measurements also yield cell size distributions. Defined air pressure is applied using pressurized air and monitored using a pressure gauge (0 - 100 kPa, Noshok Inc., Berea, OH, USA). To measure the filtrate volume, we determine the absorbance of the filtrate volume using plate reader. To rapidly optimize parameters for a particular cell type, we temporarily seal unused sections of the filtration device array by taping wells in the loading plate using laboratory paper tape (VWR).

Absorbance measurements: To quantify filtrate volumes, we measure the absorbance of the resultant cell suspensions in the 96-well collection plate. Since the cell medium contains phenol red, we measure absorbance at 560 nm using a plate reader (Infinite M1000, Tecan).

Cellular imaging: To image the cells that occlude the interpillar gaps during filtration, cells are labeled with Calcein-AM (5 µM, Invitrogen) prior to filtering through devices that are bonded to a glass coverslip. Images are acquired using a fluorescence microscope (Zeiss Observer A.1 Axio) equipped with a 10x objective (10x/EC Plan-Neofluar, 0.3 Ph1 M27, Zeiss), a light source (HBO 103W/2 mercury vapor short-arc lamp), and filter set 13 (Zeiss). To quantify % occluded gaps, we count the total number of gaps and occluded gaps.

Cell cycle analysis: To perform cell cycle analysis, adhered cells are harvested and resuspended in fresh medium to a density of 2 x 10^6 cells/mL. Cells are washed once in PBS containing 1% FBS (Gibco) by centrifugation and resuspended in 70% ethanol (Fisher Scientific) solution made in PBS. Cells are fixed in the ethanol solution overnight at -20 °C. Cells are washed once in PBS by centrifugation and stained with propidium iodide (PI) staining solution at a density of 2 x 10^6 cells/mL for 30 minutes at 37 °C. PI staining solution contains 50 ug/mL PI (Thermo Fisher Scientific), 2.5 mg/mL RNase solution (Invitrogen) in PBS. To minimize clusters of cells, cell suspensions are passed through cell strainer with 35 µm mesh size (BD Falcon) prior to analysis using flow cytometry (LSRFortessa cell analyzer, BD Falcon).

q-DC: Quantitative deformability cytometry (q-DC) is a microfluidic method that enables single-cell measurements of apparent elastic modulus, fluidity, and transit time through micron-scale constrictions[61]. To fabricate devices using soft lithography, a 10:1 w/w base to crosslinker ratio of polydimethylsiloxane (PDMS) is poured onto a master wafer. The device is subsequently bonded to a glass coverslip (1.5 thickness) using plasma treatment. Within 24 h of device fabrication, cell suspensions of 2 × 10^6 cells/mL are driven through constrictions of 9 µm (width) x 10 µm (height) by applying 55 kPa of air pressure. We capture images of cellular deformations on the millisecond timescale using a high-speed CMOS camera with a capture rate of 1600 frames/s (Vision Research, Wayne, New Jersey) that is mounted on an inverted microscope (Zeiss, Oberkochen, Germany) equipped with a 20x/0.40NA objective (Zeiss). We use a customized MATLAB code to analyse the time-dependent strain of individual cells. To determine the applied stress, we use agarose calibration particles that we fabricate using oil-in-water emulsions[61]. Stress-strain curves are obtained for single cells and a power-law rheology model is fitted to compute elastic modulus and fluidity[61].

Statistical methods: HTF results are expressed as mean ± SD. We use the Student's t-test method to analyze significance and obtain p-values. For the non-parametric distributions of apparent elastic modulus, fluidity, transit time and cell size, we use the Mann-Whitney U test to determine statistical significance.

HTF device concept

Theoretical framework. To drive the flow of cell suspension through individual filtration devices (**Fig 1A**), we apply air pressure uniformly across the array of devices. Each device contains rows of pillars spaced with an interpillar gap size that is ~2x smaller than the cell diameter; thus, while cell medium flows freely through the gaps, cells that transit through gaps are required to deform with ~40 to 60% strains[61]. If a cell does not transit, it occludes the gap (**Fig 1B**). The probability of occlusion depends on the driving pressure, filtration time, cell-to-gap size ratio, and cell deformability[28,41,42,61]. For suspensions of cells that have a similar size distribution and are filtered at a fixed driving pressure, cell deformability is a major contributor to filtration[28,41,42,64,65]: stiffer cells with higher elastic moduli tend to occlude narrow gaps more frequently than more compliant cells with lower elastic moduli[28,66,67]. While cells are in contact with the pillar surface as they transit through narrow gaps, transit is dominated by the ability of cells to deform and change shape[61,65,68,69].

To understand the physical mechanism of HT filtration, we investigate how key experimental parameters—filtration time, cell density, and driving pressure—affect the filtration of a suspension of human ovarian cancer (OVCAR5 Cis-R) cells. We first investigate the time-dependence of filtration by imaging the pillar array over the filtration time period. At timescales of 30 to 120 s, we observe there is a monotonic increase in the number of occlusions as an increasing number of cells block the interpillar gaps (**Fig 1C, D**).

To further understand the changes in fluidic resistance that occur with filtration, we perform Monte Carlo simulations to predict filtrate volume over time. We consider the filtration device as an electric circuit[70] (**Fig 1A**), where R is the fluidic resistance, P_{inlet} is the driving pressure, P_{atm} is atmospheric pressure, and Q is the resultant fluid flow:

$$P_{inlet} - P_{atm} = QR.$$

As we observe experimentally that the number of occluded gaps increases linearly as a function of time (**Fig 1D**), we model the change in fluidic resistance as a function of the number of occluded gaps,

$$R(t) \sim \frac{R_{initial}}{\left(1 - \frac{N_{occluded}}{N_{total}}\right)},$$

where R_{intial} is the initial fluidic resistance, $N_{occluded}$ is the number of occluded gaps, N_{total} is the total number of gaps, and t is time. The Monte Carlo simulation determines the filtrate volume per time by iterating through time steps of 1 ms (**Fig 1E**). As cells occlude gaps, the fluidic resistance increases, which is consistent with a modified Darcy's Law[28]. Experimental measurements of filtrate volume obtained by filtration of OVCAR5 cisplatin-resistant (Cis-R) cells are in agreement with the simulations (**Fig 1E**), which validates this model describing the filtration process.

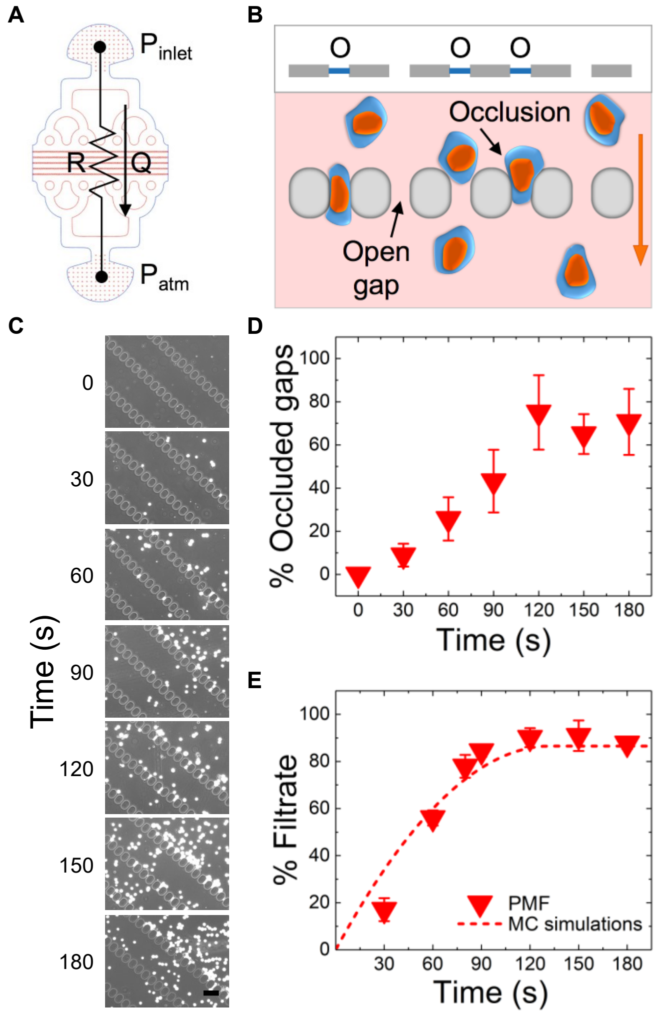

Figure 1. Defining the physical mechanism of HT filtration. (A) To simulate the filtration process, we consider the filtration device as an electric circuit, where *R* is the fluidic resistance, *Q* is the flow, P_{inlet} is the driving pressure, and P_{atm} is atmospheric pressure. (B) Schematic illustration showing simulation setup whereby fluidic resistance is determined by the number of occluded (O) versus open gaps. (C) Images of the pillar array over the filtration time. Brightfield images are overlaid with fluorescence to show OVCAR5 Cis-R cells (labeled with Calcein-AM) trapped in the array of pillars. Scale, 100 µm. (D) Quantification of occluded 10 µm gaps in HTF devices over the filtration time course for OVCAR5 Cis-R cells filtered at a driving pressure of 28 kPa and 0.5 x 10^6 cells/mL. Each data point represents mean ± SD from two independent experiments. (E) The percentage of the initial loaded volume collected as filtrate is defined as % Filtrate. Plot shows % Filtrate as a function of time. Triangles show experimental data obtained for OVCAR5 Cis-R cells filtered through 10 µm gaps at a driving pressure of 28 kPa for 90 s with 0.5 x 10^6 cells/mL. Each data point represents mean ± standard deviation (SD) over three independent experiments. Dashed line shows results of Monte Carlo (MC) simulations.

HTF device fabrication & operation

Device fabrication. To scale up the filtration assay so that multiple cell samples can be measured simultaneously, we fabricate an array of 96 microfluidic filtration devices using soft lithography. The HTF device array consists of two polydimethylsiloxane (PDMS) layers, which are each fabricated separately and then bonded together (**Fig 2A**). One PDMS layer contains the individual filtration devices that are fabricated using standard photolithography methods to have a customized array of micron-scale gaps (**Fig 2B-D**) and a height of 10 μm[71]. To produce inlets that align with 96-well plates, we use an array of 96 x 250 μL pipette tips as a mold (**Fig 2A**). The other layer contains the outlets and is fabricated by pouring PDMS onto a plain silicon wafer and casting holes using the same array of 96 pipette tips; the resultant holes are then aligned with the outlets of the devices in the upper layer. The two layers are covalently bonded together by exposing to UV light in the presence of ozone[62,72]. To enable insertion of tubing simultaneously across 96 wells, we custom-fabricate a spacer plate out of polylactic acid using 3D printing (**Fig 2E10**), and affix outlet tubing that inserts into the molded outlets of the second PDMS layer. To load samples into the devices, we fabricate a loading plate that consists of a 96-well plate with protrusions at the bottom of each well (**Fig 2E6**), which insert directly into the inlet holes of the top PDMS layer (**Fig 2E9**). The assembled two-layer HTF device array with the attached loading and spacer plates is inserted into a custom-built plate holder (**Fig 2E8**), which is placed on top of a standard 96-well plate (**Fig 2E11**) in which the filtrate is collected. While we demonstrate here fabrication of a 96-array device, the procedure is scalable and could be modified to generate arrays of devices that interface with a range of plate sizes from 24 to 384-wells. Importantly, the customizable architecture of the HTF device enables fabrication of device arrays that have a range of gap sizes, which can enable rapid determination of the optimal gap size for filtration in a single experiment.

Device operation. To load the device, suspensions of cells in media are transferred into the loading plate using a 96-pin multichannel head. To apply uniform air pressure to drive cell suspensions through the filtration devices uniformly across the device array, we secure a pressure chamber (**Fig 2E2**) on top of the plate holder using clamps (**Fig 2E5**); placement of a rubber sealing pad (**Fig 2E4**) between the holder and the pressure chamber ensures air-tight sealing. To apply a well-defined magnitude of positive air pressure we use compressed air (via **Fig 2E3**), which is monitored using a pressure gauge (**Fig 2E1**), as displayed in **Fig 2F**. Upon applying air pressure, the cell suspensions are driven to enter into each device; the resultant filtrate containing cells and media that have filtered through the device is measured by determining the absorbance of phenol red (560 nm), which is contained in the cell media, as an indicator of filtrate volume; such measurements can be obtained using a plate reader in a multiwell plate format. To equate absorbance and filtrate volume, we generate a standard curve and confirm that the presence of cells in the media has no effect on absorbance (**Supp Fig 1A**), substantiating that absorbance measurements can be used to reliably report filtration volume.

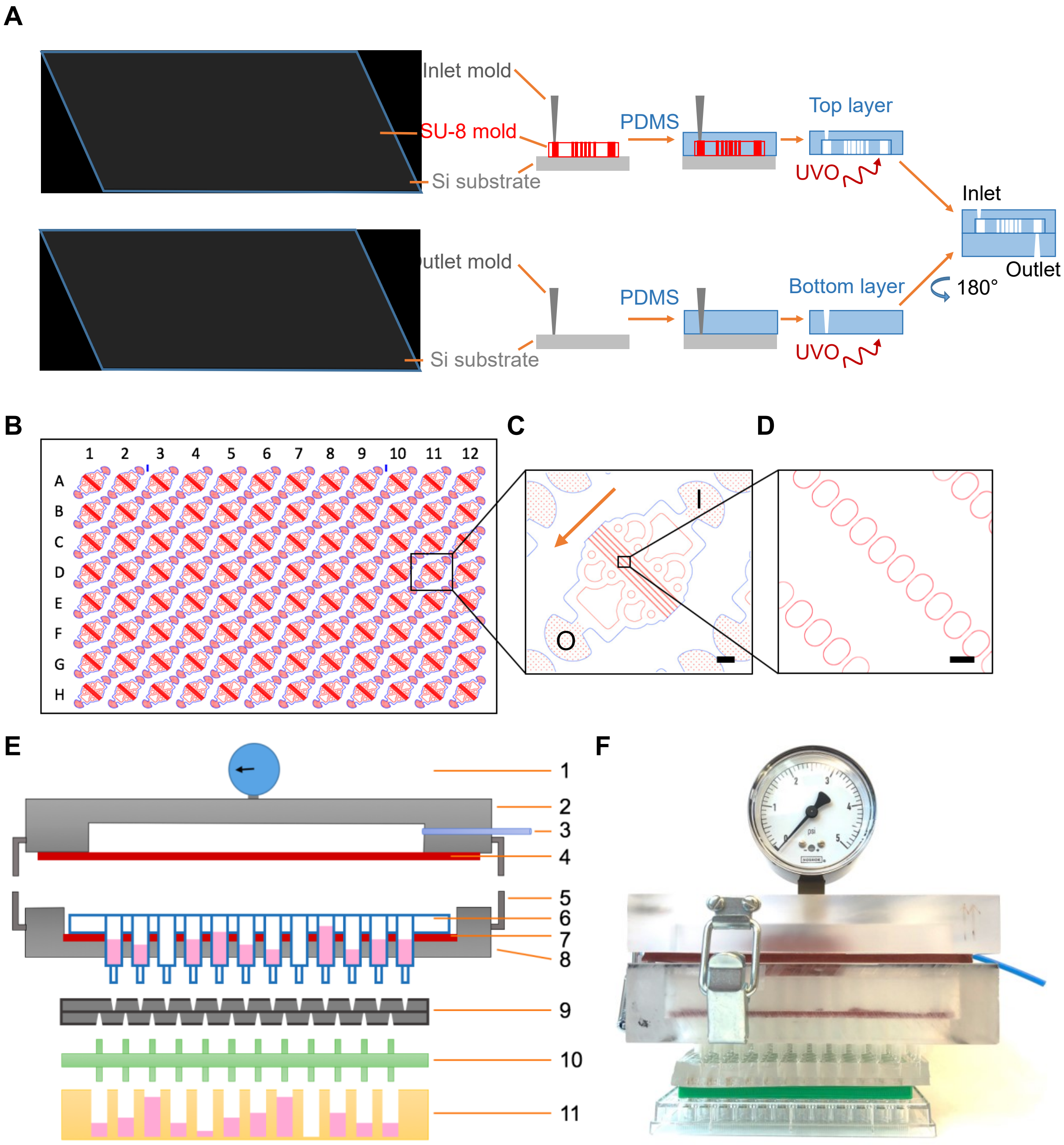

Figure 2. Architecture of the HTF system. (A) Schematic showing fabrication of the two-layer PDMS array of devices that is fabricated by bonding together top and bottom PDMS layers. Inlets and outlets are molded using a standard 96-array of pipette tips. (B) Plan view of array of 96 filtration devices. Inset shows: (C) single filtration device. Arrow indicates direction of fluid flow from inlet (I) to outlet (O). Scale, 1 mm. Inset shows: (D) array of pillars with defined interpillar gap size through which cells are filtered. Scale, 100 µm. (E) Schematic of HTF system: 1. Pressure gauge; 2. Pressure chamber; 3. Connection to pressure source; 4. Rubber sealing pad; 5. Clamps; 6. Loading plate; 7. Rubber sealing pad; 8. Custom fabricated plate holder; 9. PDMS array of devices; 10. Spacer plate with affixed tubing; 11. Standard 96 well filtrate collection plate. (F) Photo of the HTF system.

Results and Discussion

Optimizing conditions for the HTF assay

We first demonstrate the process of optimizing HTF for a single cell type using OVCAR5 Cis-R cells for proof-of-concept. A key parameter for cell filtration is the gap size. The magnitude of filtration at a given pressure and time depends on the probability that cells will occlude the gaps, which is determined by cell deformability and cell size relative to the gap size[63,66]. When the gap size is larger than the cell diameter, no deformation is required for cells to flow through the gaps. When the gap size is smaller than the cell size, cells are required to deform through the gap. With increasingly smaller gaps there is increasing probability of occlusion. We previously established filtration conditions for OVCAR5 Cis-R cells with 10 μm pore membranes that yield a filtrate volume of ~40-60%[28]; this is optimal to simultaneously detect samples with both increased or decreased filtration in a parallel assay. Therefore, we use HTF devices with 10 μm gap size to optimize cell density and filtration pressure for these OVCAR5 Cis-R cells.

Since the number of cells flowing through the pillars per volume per time sets the rate of occlusion, filtration measurements are sensitive to cell density[28]. With a low cell density there are fewer occlusions and thus minimal changes to fluidic resistance, which precludes differential measurements between samples. By contrast, with higher cell densities, cells may cluster at the interpillar gaps, which can be observed over longer filtration times (**Fig 1C**); such clustering can result in decreased filtrate volume but may be sensitive to cell-cell interactions rather than single cell deformability. To determine the optimal cell density for filtration of human ovarian cancer cells, we assess the filtration of OVCAR5 Cis-R cells over a range of cell densities from 0.1 x 10^6 to 3.0 x 10^6 cells/mL at a fixed filtration pressure and time (28 kPa, 90 s). With increasing cell density, we observe a reduction in absorbance indicating decreased filtrate volume (**Supp Fig 1B**); this is consistent with the higher probability of occlusion and subsequent increased fluidic resistance. With cell densities > 1.5 x 10^6 cells/mL, we find there are no further observable changes in filtration, reflecting significant occlusion of interpillar gaps. At densities < 0.3×10^6 cells/mL, we observe 88.5 ± 4.9% filtrate; since the dead volume of the device is ~44 μL, this is the maximum measurable filtrate. Based on these findings, we determine the optimal cell density for filtration of human ovarian cancer cells is 0.5×10^6 cells/mL; at this density a sufficient number of occlusions occurs to yield a measurable filtrate while requiring the minimal number of cells.

Another essential parameter in filtration is the driving pressure, which drives fluid flow and thus impacts the number of cells that arrive at the pillars per unit time. The driving pressure must be sufficient to generate flow of cell suspension through the array of pillars, yet not excessive to completely filter the sample volume, which would preclude differential filtration measurements. To define the optimal driving pressure for OVCAR5 Cis-R cells, we conduct a pressure sweep from 14 kPa to 35 kPa. With increasing driving pressure, we observe increased filtration, with % filtrate values that range from 41.4 to 88.5% (**Supp Fig 1C**). The driving pressure for a particular experiment should be set according to the goals of the screen. For example, to design a screen where desired hits increase cell deformability, a control filtrate value around ~20% will ensure detection of compounds that result in the largest increase in % filtrate; to identify compounds that decrease cell deformability and thereby lower % filtrate, the control % filtrate should be ~80%. It is important to note that to rapidly optimize pressure, time, and gap size for a particular cell type, sections of the customized 96-device array can be used by temporarily sealing unused wells in the loading plate using laboratory paper tape. Moreover, while we show optimization of HTF parameters for OVCAR5 Cis-R cells, the settings can be readily applied to other cancer cell types with similar cell size distributions (cell to gap size ratio from ~1.3 to 1.8).

We next demonstrate the optimization of HTF to maximize the difference in readouts between 2 cell samples. As proof-of-concept, we establish conditions for HTF to distinguish between the OVCAR5 Cis-R and OVCAR5 Cis-S cells, which we previously found have distinct filtration properties using the parallel microfiltration prototype device[28]. We first optimize driving pressure to maximize the difference in % filtrate between OVCAR5 Cis-S and Cis-R cells. The optimal driving pressure should maximize the difference in filtration between cell types within the range of ~7 to 88% filtrate, which is the dynamic range of filtrate measurements. To establish the optimal driving pressure for OVCAR5 Cis-S and Cis-R cells, we perform a pressure sweep from 14 kPa to 35 kPa at a fixed filtration time of 90 s (**Supp Fig 1C**). We find the Cis-R cells have higher % filtrate than Cis-S cells, consistent with our previous observations of the increased filtration of Cis-R versus Cis-S cells through the 10 μm-pores of a polycarbonate membrane[28]. As we observe the maximum difference in filtrate between OVCAR5 Cis-S and Cis-R at 28 kPa, we select this driving pressure for subsequent experiments. The observed differential filtration of OVCAR5 Cis-S versus Cis-R cells reflects a difference in how these cells deform through narrow gaps. A difference in cell size could impact filtration, however, comparisons of cell size distributions between Cis-S and Cis-R cells reveal no significant differences (**Supp Fig 2A**), indicating that cell size alone cannot explain the differential filtration. Cell physical properties also vary with stages of the cell cycle[49,73], however, we find no significant differences in cell cycle stage between Cis-R and Cis-S cells (**Supp Fig 2B**).

HTF is sensitive to cell deformability

To test the effects of cell deformability on filtration of OVCAR5 Cis-R and Cis-S cells, we pharmacologically perturb the cytoskeleton by treating cells with paclitaxel, which stabilizes microtubules and causes cells to be stiffer[28,34,35]. We find that treatment of OVCAR5 Cis-R cells with 0.1 μM paclitaxel results in a reduction of % filtrate to 23.5 ± 9.7% compared to vehicle control of 87.6 ± 4.9% ($p = 5.3 \times 10^{-4}$) (**Fig 3B**); this is consistent with increased cell stiffness following paclitaxel treatment. We also observe a smaller but significant reduction in filtrate of paclitaxel-treated OVCAR5 Cis-S cells from 34.1 ± 15.4% to 15.8 ± 5.8% ($p = 9.0 \times 10^{-4}$); this smaller effect may be attributed to the narrow range for decrease in filtrate absorbance in the lower end of the dynamic range. We verify that paclitaxel treatment does not have a significant effect on size of the Cis-R and Cis-S cells, indicating that differential filtration of these paclitaxel-treated cells reflects changes in cell deformability (**Supp Fig 2C)**.

To confirm the distinct mechanical properties of the OVCAR5 Cis-R and Cis-S cells using an independent method, we measure the apparent elastic modulus (E_a), fluidity (β), and transit time (TT) of these cells through micron-scale constrictions of a microfluidic device using quantitative deformability cytometry (q-DC)[61]. We find that Cis-R cells have a ~21.9% lower E_a (**Fig 3C, D**) and ~10.0% increased β compared to Cis-S cells (**Fig 3E, F**), indicating they are more compliant (median $E_{a\_Cis\text{-}R}$ = 1.32 kPa versus $E_{a\_Cis\text{-}S}$ = 1.69 kPa , $p = 1.4 \times 10^{-8}$; median $\beta_{Cis\text{-}R}$ = 0.33 versus $\beta_{Cis\text{-}S}$ = 0.30, $p = 3.9 \times 10^{-6}$). Cis-R cells also exhibit a faster transit time through micron-scale constrictions compared to Cis-S cells (median $TT_{Cis\text{-}R}$ = 15.0 ms versus $TT_{Cis\text{-}S}$ = 34.8 ms, $p = 3.9 \times 10^{-33}$) (**Fig 3G, H**). Since measurements of E_a and β using q-DC are sensitive to the magnitude of deformation[61], and the constriction size is fixed, these measurements could also be sensitive to cell size; however, we find no significant correlation between the measured cell diameters (d) and q-DC measurements (Pearson's r: $(E_a\ vs\ d)_{Cis\text{-}R\_}$ = 0.0, $(E_a\ vs\ d)_{Cis\text{-}S}$ = 0.0; $(\beta\ vs\ d)_{Cis\text{-}R}$ = -0.1, $(\beta\ vs\ d)_{Cis\text{-}S}$ = 0.0; $(TT\ vs\ d)_{Cis\text{-}R}$ = 0.0, $(TT\ vs\ d)_{Cis\text{-}S}$ = 0.1). Taken together, these findings substantiate that differences in cell deformability can be detected by differences in % filtrate using HTF.

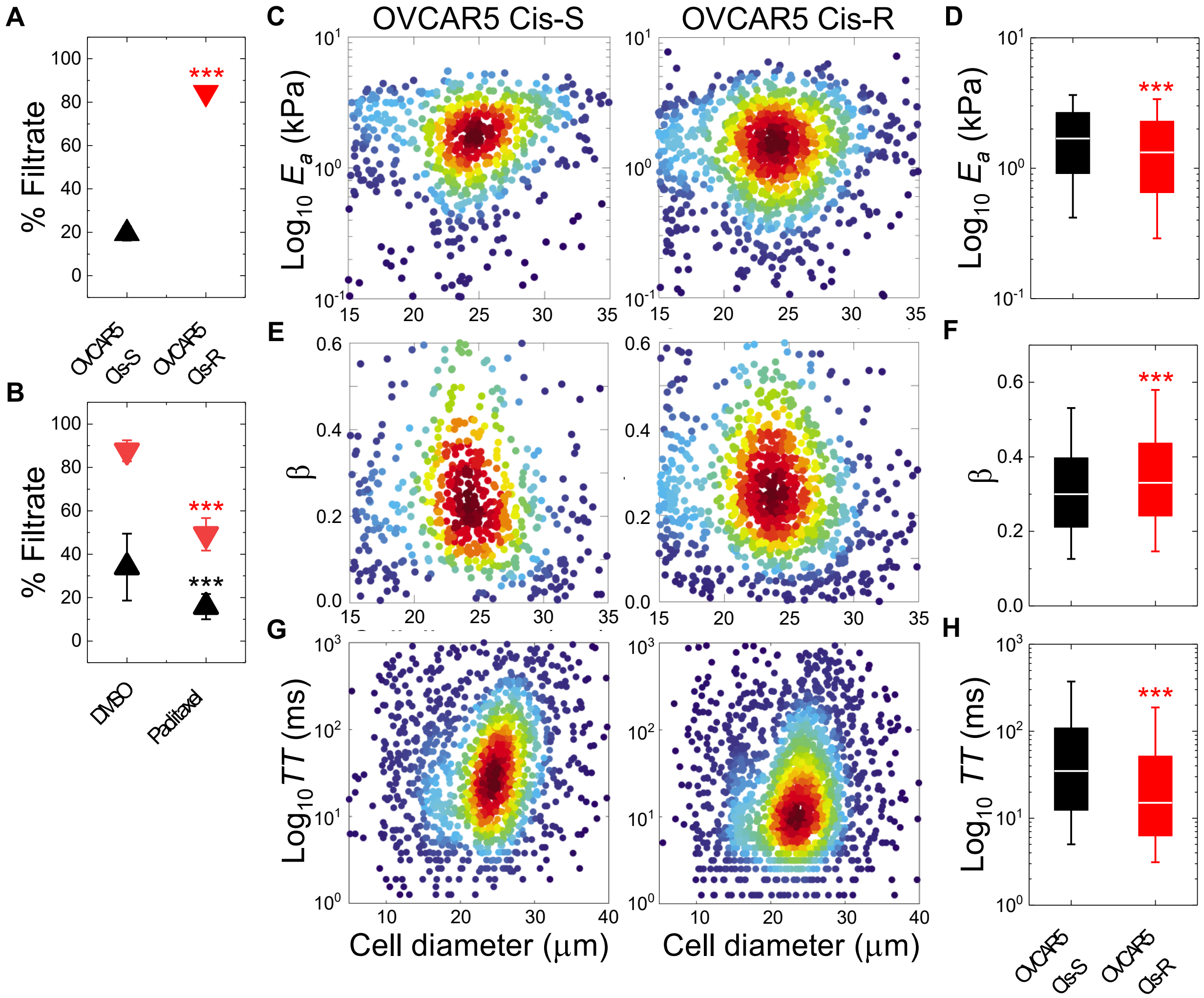

Figure 3. HTF is sensitive to cell deformability. (A) Differential filtration of human ovarian cancer OVCAR5 Cis-R and Cis-S cells and (B) OVCAR5 Cis-R and Cis-S cells treated with 0.1 µM of the microtubule-stabilizing drug paclitaxel for 24 h prior to filtration through 10 µm gaps at 28 kPa, 90 s, and 0.5 x 10^6 cells/mL. Data points in A and B represent mean ± SD from three independent experiments. Statistical significance is determined using student's t-test. (C) Density scatter plots for measurements of apparent cell elastic modulus (E_a) using quantitative deformability cytometry (q-DC). Each dot represents a single cell. N > 700 per sample. (D) Box plots showing E_a measurements. (E) Density scatter plots for measurements of cell fluidity (β) using q-DC. Each dot represents a single cell. N > 700 per sample. (F) Box plots showing β measurements. (G) Density scatter plots for measurements of cell transit time (*TT*) using q-DC. Each dot represents a single cell. N > 1300 per sample. (H) Box plots showing *TT* measurements. Box plots show the 25th and 75th percentiles; whiskers denote 10th and 90th percentiles; and line is the median. Statistical significance is determined using the Mann Whitney U test. *** $p < 0.001$; ** $p < 0.01$; * $p < 0.05$.

Resolving cell types based on differential filtration

To validate HTF to measure differences in filtration based on cell deformability, we investigate a set of three cell lines that represent both epithelial- and mesenchymal-like phenotypes. EMT is implicated in cancer progression and metastasis, as mesenchymal-type cells tend to be more motile and invasive[44]. We and others previously showed that mesenchymal-type cells are more deformable than epithelial-type cells[28,74]. To investigate the filtration of epithelial- and mesenchymal-type cells using HTF, we compare human ovarian cancer (OVCA433) cells that are epithelial-type (OVCA433 GFP) and mesenchymal-type by transforming cells to overexpress genes (SNAI1, SNAI2) that are master regulators of EMT (OVCA433 Snail, OVCA433 Slug)[28].

To determine HTF conditions that maximize the difference in filtrate between epithelial-type control (OVCA433 GFP) cells and mesenchymal-type (OVCA433 Snail, OVCA433 Slug) cells, we first confirm the optimal interpillar gap size. Given the median cell size of 15 μm for OVCAR433 GFP, OVCAR433 Slug, and OVCAR433 Snail cells (**Supp Fig 2D**), we investigate filtration through devices with varying interpillar gap sizes from 6 to 14 μm within a single 'calibration' experiment (**Fig 4A**). Our findings confirm that a gap size of 10 μm achieves the largest difference in filtrate volume between epithelial and mesenchymal-type cells at a fixed driving pressure of 28 kPa and 60 s filtration time ($p_{Snail} = 9.6 \times 10^{-4}$, $p_{Slug} = 3.0 \times 10^{-3}$) (**Fig 4B**). We observe no significant differences in cell size distributions for these cells (**Supp Fig 2D**), thereby excluding differences in size as a cause of the differential filtration. We find no significant differences in cell cycle stage among these cell lines (**Supp Fig 2E**), which could also impact cell deformability[49,73]. We also observe no differences in filtration of these cells with or without surfactant (Pluronics F-127) (**Supp Fig 2F**), which minimizes cell-PDMS interactions[63]; these findings are consistent with previous observations that the ability of cells to transit through micron-scale pores is largely determined by cell deformability rather than surface effects on these ~90 s timescales[61,65,68,69]. Another possible origin of the decreased filtrate of the epithelial-type cells may be increased cell-cell interactions; however, we previously found that despite the higher E-cadherin expression of OVCA433 GFP cells compared to OVCA433 Snail and Slug, there were no significant differences in cell clustering on the timescales of these filtration measurements[28]. Taken together, these observations suggest the increased filtration of the mesenchymal-type cells reflects their increased deformability. More broadly, this process of optimizing gap size to maximize resolution between samples within a single calibration experiment provides a framework for adapting HTF to new cell types and screening applications.

To further investigate the applicability of HTF to other cell types, we conduct filtration experiments with human breast cancer cells including malignant triple negative (MDA-MB-468 and MDA-MB-231) as well as immortalized benign (MCF10A) cells[75]. Given the similar size distributions of the breast and ovarian cell lines (**Supp Fig 2A, D, G**), we first tested the same HTF conditions as optimized for the ovarian cancer cell lines (10 μm gap, 28 kPa for 60 s). With these conditions, we observe a significant ~10.4 to 33.5% increased filtrate for malignant breast cancer cells compared to the benign cells ($p_{\text{MDA-MB-468}} = 1.3 \times 10^{-2}$; $p_{\text{MDA-MB-231}} = 1.7 \times 10^{-5}$) indicating that the malignant cells are more deformable than the benign cells (**Fig 4C**). These observations are consistent with previous reports that malignant human cell lines[40,76,77] and cells from patient pleural effusions[47] have a reduced elastic modulus compared to benign cells. We also confirm the effect of pharmacological perturbation of the cytoskeleton by treatment of malignant MDA-MB-231 cells with 0.1 μM paclitaxel, which results in a reduction of % filtrate to 39.3 ± 10.3% compared to vehicle control of 66.4 ± 3.2% ($p = 1.4 \times 10^{-3}$) (**Fig 4D**); this is in line with the effect of paclitaxel on filtration of OVCAR5 Cis-R and Cis-S cells. We verify that the observed reduction in filtrate is not due to the effect of paclitaxel on the size of MDA-MB-231 cells, indicating that differential filtration of paclitaxel-treated cells reflects changes in cell deformability (**Supp Fig 2H)**.

We additionally filter weakly metastatic prostate cancer (DU145) cells in parallel with highly metastatic cells that we generated by knockdown of the nuclear envelope protein, emerin (DU145 Emerin KD)[78]. As these prostate cancer cells have a similar size distribution as the other cell types (**Supp Fig 2A, D, I**), we also tested the same filtration settings as for the ovarian cancer cells. We find that the highly metastatic cells with emerin KD have increased % filtrate (61.1 ± 13.9%) compared to the untransformed, weakly metastatic cells (17.0 ± 11.1%) ($p_{DU145\ Emerin\ KD} = 1.4 \times 10^{-6}$) (**Fig 4E**). These observations using HTF are consistent with previous findings of altered nuclear mechanical stability with reduced levels of emerin[79,80], including our previous study using the prototype PMF device[81]; notably, downregulation of emerin promotes malignant transformation of cancer cells[81]. Taken together, these observations confirm the application of HTF for screening cells that derive from distinct tissues.

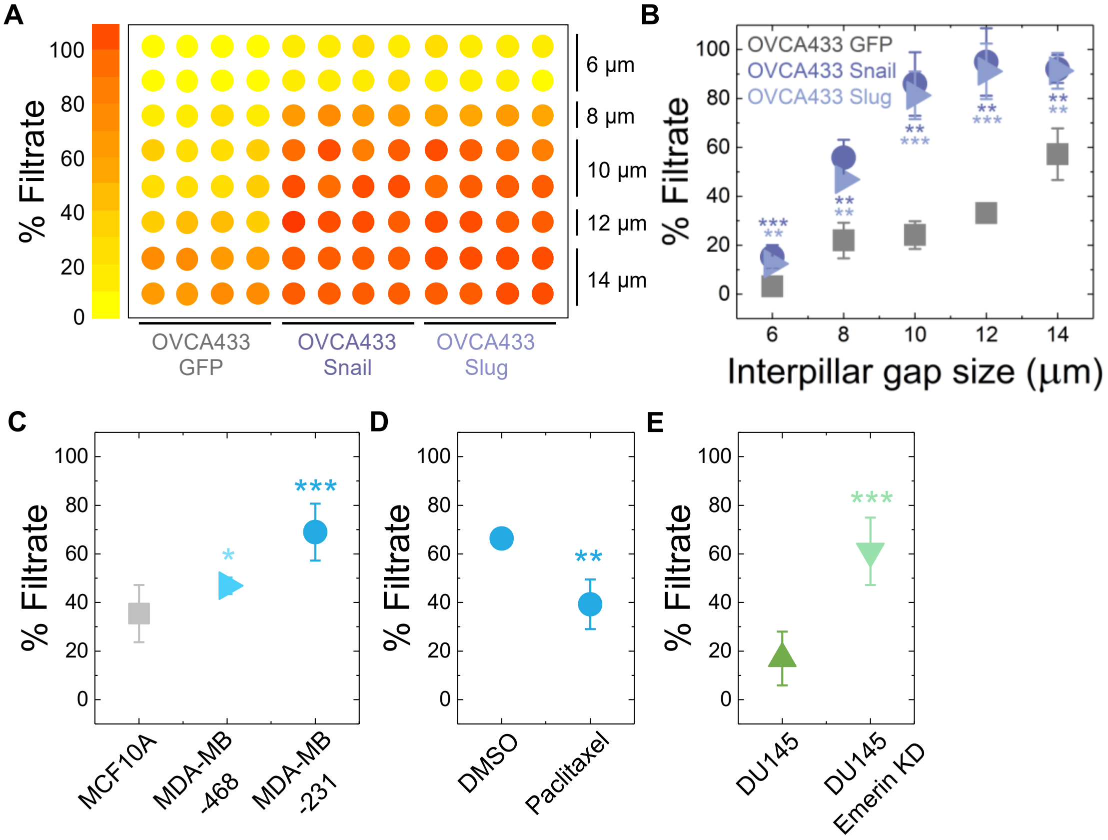

Figure 4. Using HTF to distinguish cell types. (A) Heat map of % filtrate for epithelial- (GFP) versus mesenchymal-type (Snail, Slug) human ovarian cancer (OVCA433) cells with different interpillar gap sizes in parallel. (B) % Filtrate versus gap size for OVCA433 cells. (C) Differential filtration of human breast cancer cells (MDA-MB-468, MDA-MB-231) and normal breast epithelial (MCF10A) cells. (D) MDA-MB-231 cells treated with 0.1 µM of paclitaxel for 24 h prior to filtration. (E) Differential filtration of human prostate cancer cells that are weakly metastatic (DU145) and transformed by knockdown [82] of emerin to be highly metastatic (DU145 Emerin KD). Filtration through 10 µm gaps at 28 kPa, 60 s, and 0.5 x 10^6 cells/mL for all cell types. Data points represent mean ± SD from three independent experiments and statistical significance is determined using student's t-test. *** $p < 0.001$; ** $p < 0.01$; * $p < 0.05$.

Cell filtration is sensitive to cytoskeletal and nuclear perturbations

To establish the role of molecular mediators of cellular deformability in regulating filtration, we treat the EMT panel of human ovarian cancer (OVCA433 GFP, OVCA433 Snail, and OVCA433 Slug) cells with compounds that are well established to alter cell and nuclear mechanical properties and/or mechanosignaling pathways (**Fig 5**). Such pharmacological perturbations are commonly used to validate that a new mechanotyping technology is sensitive to changes in cell physical properties[28,51,83]. To perturb the cytoskeleton, we treat cells with compounds to inhibit actin polymerization (cytochalasin D), activate actin polymerization (colchicine), stabilize microtubules (paclitaxel), and inhibit myosin II activity (blebbistatin). We also treat cells with additional compounds that are known to alter cell mechanotype through signaling pathways that result in cytoskeletal changes including inhibitors of transforming growth factor (TGF)-β (SB43154) and the yes-associated-protein (YAP) transcription factor (verteporfin), which is implicated in cellular mechanosensing at the scale of tissues and organs[84,85]. To further investigate the effects of nuclear physical properties on cell filtration, we treat cells with the histone deacetylase inhibitor (trichostatin-A), which is established to make cell nuclei more deformable[86].

Using the filtration conditions established to maximize the difference in filtrate volume between the epithelial- and mesenchymal-type cells, the OVCA433 Snail and Slug mesenchymal-type cells exhibit 77.3 ± 5.8% and 80.2 ± 8.0% filtrate whereas the reference filtrate for DMSO treated OVCA433 GFP control, epithelial-type cells is 22.6 ± 4.4%. In a screen including these three cell types, it is thus possible to identify compounds that increase filtrate volume for the epithelial-type OVCA433 GFP cells and decrease filtrate of the mesenchymal-type OVCA433 cells overexpressing Snail and Slug cells, which have reference filtrates of 77.3% and 80.2% that are close to the upper limit of ~88% filtrate.

As shown in **Fig 5**, we find that cytoskeletal-perturbing drugs consistently alter cell filtration. We first investigate actin, which is a major component of the cytoskeleton; the organization and levels of filamentous[87] actin are key determinants of cell deformability[28,40]. To inhibit polymerization of F-actin, we treat cells with cytochalasin D[88]; this results in a significant increase in % filtrate for the OVCA433 GFP cells to 81.6 ± 8.7% ($p = 4.4 \times 10^{-4}$), which is consistent with observations that inhibiting actin polymerization makes cells more deformable[89,90]. We also observe slight increases in filtrate for OVCA433 Slug to 86.7 ± 3.6% ($p = 5.7 \times 10^{-2}$) and OVCA433 Snail cells to 85.3 ± 6.6% ($p = 8.3 \times 10^{-2}$); the reduced effects of cytochalasin D treatment on the filtration of mesenchymal-type cells reflect the initial filtrates near the upper limit of 77.3% and 80.2% for OVCA433 Snail and Slug cells, which precludes measurements of larger increases in filtrate. By contrast, activating polymerization of F-actin with 10 μM colchicine[91] induces a significant decrease in filtrate of mesenchymal-type cells to 37.2 ± 2.9% for Snail and 39.4 ± 3.7% to Slug cells ($p_{Snail} = 1.5 \times 10^{-3}$, $p_{Slug} = 1.7 \times 10^{-3}$); these observations are aligned with previous findings of decreased cell deformability with this concentration of drug[28,35,92]. As the reference filtrate of OVCA433 GFP cells is 19.7 ± 3.3%, we do not detect any further significant reduction in filtration of these cells with colchicine treatment (**Fig 5**). Together these findings confirm the effects of actin cytoskeleton organization on filtration volume, which further validates HTF as a method to detect differences in cell deformability.

Another major cytoskeletal component is microtubules. To stabilize microtubules, we treat cells with paclitaxel[35,93]. Following this treatment, we observe significant reductions in % filtrate for OVCA433 EMT-transformed cells to 15.3 ± 6.6% and 17.5 ± 5.8% ($p_{Snail} = 1.5 \times 10^{-4}$, $p_{Slug} = 2.9 \times 10^{-4}$), compared to vehicle treatment. We also find a smaller but significant decrease in filtrate of the OVCA433 GFP cells to 9.5 ± 2.9%, ($p = 0.13 \times 10^{-2}$), which is expected as the initial filtrate for these cells is already approaching the lower end of the dynamic range. These findings are aligned with previous results that paclitaxel decreases cellular deformability[28,34,35].

Nonmuscle myosin II (NMII) is an important determinant of cell mechanotype as this protein crosslinks actin filaments and is implicated in generating physical forces that contribute to intracellular tension[94-96]. To determine the effects of NMII activity on filtration, we treat cells with the NMII inhibitor blebbistatin. We observe a slight increase in % filtrate for OVCA433 Snail to 86.0 ± 2.2% (p_{Snail} = 7.2 x 10^{-2}) and OVCA433 Slug to 84.5 ± 2.9% (p_{Slug} = 8.6 x 10^{-2}), indicating decreased cell deformability; these findings are consistent with previous reports that inhibiting NMII activity for cells in a suspended state causes them to be stiffer[94], which may be explained by the reduction in myosin-mediated actin disassembly and remodeling[97]. There is no significant decrease in filtration of OVCA433 GFP cells with inhibition of NMII activity (p = 7.3 x 10^{-2}), suggesting that NMII activity may play a different role in regulating the mechanotype of epithelial-type cells.

Two other pathways that regulate actin organization are mediated through TGF-β[98,99] and YAP[100,101]. Activation of TGF-β promotes actin stress fiber formation[98,102] and EMT[103,104]. However, we find no significant changes in % filtrate of epithelial- and mesenchymal-type OVCA433 cells with the TGF-β inhibitor SB431542, indicating that inhibiting endogenous TGF-β activity does not affect cell filtration. These findings contrast previous studies that report increased cell deformability with activation of TGF-β[105,106]; however, in those studies, cells were grown in the presence of TGF-β supplementation, whereas we assess here effects of the inhibitor without additional activation of TGF-β. To investigate the role of YAP activity, we treat cells with the YAP inhibitor, verteporfin. Loss of YAP activity leads to stabilization of actin filaments via RhoA GTPase[100,101]. We find that verteporfin treatment reduces the filtration of mesenchymal-type cells to 66.3 ± 1.5% for OVCA433 Snail (p_{Snail} = 6.2 x 10^{-2}) and to 63.4 ± 4.4% for OVCA433 Slug (p_{Slug} = 2.2 x 10^{-2}), which is consistent with a reduction in cell deformability due to YAP inhibition. We find no significant change in filtration for OVCA433 GFP with verteporfin (p = 9.8 x 10^{-1}), which is likely due to the lower limit of the dynamic range. While verteporfin may have additional off target effects[107,108], these observations are consistent with previous reports that loss of YAP activity results in cell stiffening through increased F-actin[100,101].

We next investigate the effect of nuclear perturbation on cell filtration. The nucleus is typically the stiffest and largest organelle, which rate-limits the deformation of cells through narrow gaps[109,110]. To determine effects of nuclear structure on cell filtration, we treat cells with the histone deacetylase (HDAC) inhibitor, trichostatin A, which causes chromatin decondensation[111,112]. Treatment of cells with trichostatin A leads to increased % filtrate across both epithelial- and mesenchymal-type cells compared to vehicle control ($p_{Snail} = 9.1 \times 10^{-2}$, $p_{Slug} = 7.2 \times 10^{-2}$, $p_{GFP} = 3.7 \times 10^{-4}$), indicating that the structural organization of the nucleus contributes to cell filtration (**Fig 5**). These findings are consistent with a previous report showing enhanced deformability of cell nuclei in intact cells with trichostatin A treatment[86]. Taken together, filtration of cells treated with this panel of compounds indicates that HTF is sensitive to perturbations of cytoskeletal and nuclear components.

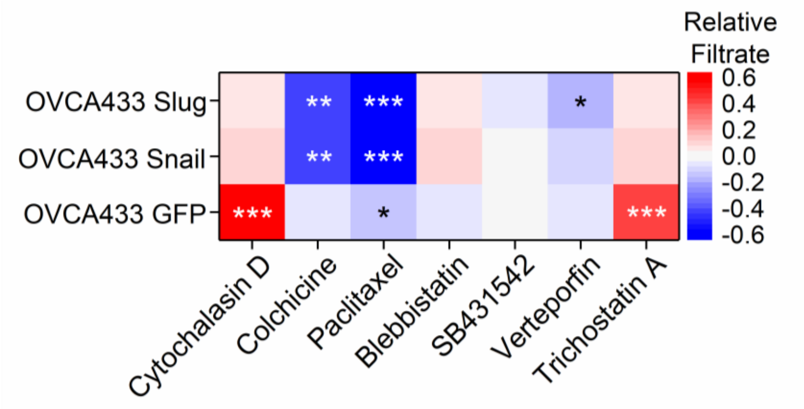

Figure 5. Effects of pharmacologic perturbations to cytoskeleton and nucleus on filtration. Treatment of OVCA433 (GFP, Snail, Slug) cells with a panel of drugs: actin polymerization inhibitor (cytochalasin D), actin polymerization activator (colchicine), microtubule stabilizer (paclitaxel), myosin II activity inhibitor (blebbistatin), TGF-β inhibitor (SB431542), YAP inhibitor (verteporfin), HDAC inhibitor (trichostatin A). All treatments at 10 μM for 24 h prior to filtration. Color represents filtrate relative to the DMSO treated cells. Filtration through 10 μm gap size at 28 kPa for 60 s, and 0.5×10^6 cells/mL. Statistical significance compared to the DMSO treated control is determined using student's t-test. *** $p < 0.001$; ** $p < 0.01$; * $p < 0.05$.

To assess the quality of the HTF assay, we first characterize the variability in % filtrate measurements. The variability in % filtrate of media without any cells filtered through HTF device arrays is indicated by the SD of ± 6.6% with gap size of 10 μm, for 20 s at 28 kPa (**Supp Fig 3A**). For filtration of human ovarian cancer (OVCA433) cells we observe a SD of ± 10.6% in % filtrate across device arrays with a confidence interval of -0.6 to 20.4% using filtration conditions of 10 μm gap size, 28 kPa for 60 s and 0.5 x 10^6 cells/mL (**Supp Fig 3B**).

To further assess the quality of the HTF assay for a higher throughput screen, we use the filtration results across the panel of cytoskeletal and nuclear perturbing compounds (**Fig 5**): this enables us to evaluate the *Z'*-factor, which provides a metric for evaluating the statistical robustness of filtration measurements based on the difference in maximum and minimum readouts[113]. The *Z'*-factor reflects the dynamic range of HTF measurements and also accounts for data variation as it is determined by the mean and standard deviation of drug treated samples with maximum (μ_{c+} ,σ_{c+}) and minimum (μ_{c-} ,σ_{c-}) filtrates for each cell type,

$$Z' = 1 - \frac{(3\sigma_{max} + 3\sigma_{min})}{|\mu_{max} - \mu_{min}|}.$$

A value of $Z' > 0.5$ is an indication of high assay quality. As proof-of-concept, we use data of OVCA433 GFP cells treated with cytochalasin D that exhibits maximum filtrate and with paclitaxel that results in the minimum filtrate; each of these compounds are established to increase and decrease cellular deformability, respectively[28]; the resultant $Z' = 0.61$ for the OVCA433 GFP cells. We also determine *Z'* values of 0.63 for OVCA433 Snail and 0.61 OVCA433 Slug cells, reflecting the good quality of the HTF assay. While the *Z'*-factor provides a metric to evaluate assay quality without intervention of test compounds, we further assess the suitability of HTF for a higher throughput screen to identify hit compounds that modulate cell deformability by evaluating the *Z*-factor[113],

$$Z = 1 - \frac{(3\sigma_s + 3\sigma_c)}{|\mu_s - \mu_c|},$$

where μ_s, σ_s are the sample mean and standard deviation, and μ_c, σ_c are the control mean/standard deviation. For an ideal HT assay, $Z = 1$, while $0.5 < Z < 1$ indicates an excellent assay with greater likelihood of identifying statistically robust hits; by contrast, $Z < 0$ indicates that the screen will not yield any meaningful results. Envisioning a screen to identify hits that cause mesenchymal-type cells to become less invasive, and thereby less deformable, we consider the untreated cells as the control and the paclitaxel-treated cells as the sample; this yields $Z = 0.34$ to 0.40. For a screen to identify hits that cause OVCA433 GFP epithelial-type cells to become more deformable, we consider untreated OVCA433 GFP as the control and cytochalasin D-treated cells as the sample, which yields $Z = 0.34$. While these are relatively low Z-factors for a high quality HT screen, values of Z' and $Z > 0$ indicate that the assay is functional and further optimization is needed to successfully configure HTF for a particular HT screen[113].

One strategy to improve the Z-factor is to reduce filtrate variability between devices; this could be achieved by optimizing device geometry to minimize the presence of air bubbles or other factors that cause variability in flow during filtration. Another strategy to increase the Z-factor is to reduce the dead volume of the HTF setup; this sets the upper limit of measurable filtrate volume and thus dynamic range of HTF measurements. Into the future, injection molding[114] or micromachining[57,115] may enable more consistent fabrication of filtration devices that also eliminate the need for separate components such as loading and outlet plates. Additional future analysis is required to precisely define how sensitive HTF is to small changes in cell elastic modulus by filtration of calibration particles or cells treated with a compound that results in known changes in cell stiffness; in this way, the sensitivity of filtration volume to changes in elastic modulus could be precisely quantified.

As with all HT-screening methods, the power of HTF lies in the ability to rapidly screen samples using a readout that is quick, user-friendly, and inexpensive to obtain. Top ‘hit’ compounds can be identified based on their ability to induce the largest changes in filtrate volume. We show here that filtration is modulated by cell deformability. However, other factors, such as cell size, cell cycle stage, cell-cell clustering, and density of the cell suspension, also regulate filtration. Validation of top hits in greater detail using secondary orthogonal assays can be used to select hits for the desired trait(s) that impact filtration.

With the challenges in identifying effective treatment strategies for cancer, cell filtration provides an elegant way to screen cells in a way that complements specific molecular biomarkers, such as E-cadherin and vimentin for EMT-status[116], EpCAM and MUC-1 for cancer stem cells[117], or Ki67 for cell proliferation[118]. We show here that filtration is sensitive to the altered deformability of chemoresistant cancer cells as well as epithelial- versus mesenchymal-type cancer cells, which have distinct mechanical properties[74]. Cancer cell deformability shows strong associations with invasion in many contexts[29,40,77,119], and may have functional consequences in metastasis where cells are required to undergo large deformations[25,110]. Molecular mediators that regulate mechanotype also generate forces required for cell movement and shape changes[120]. Thus, HTF could be a complementary tool for drug discovery that harnesses cell deformability as a surrogate phenotype to rapidly evaluate the effects of drugs or novel genes to inhibit invasion. HTF could also be used to address basic research questions through a Crispr/Cas9 or shRNA screen to define molecular mediators of cell deformability. While we envision HTF is amenable to screening established cell lines and/or patient-derived cells, future efforts to scale down the device volume could enable testing of primary patient samples. A distinct advantage of HTF is that the assay requires minutes to assess cell deformability using filtration; by contrast, existing methods that screen based on cell invasion, motility, or even proliferation, require 10-100 hours per assay[12,13,121]. While HTF offers these unique advantages, complementary assays to measure other factors that may contribute to cell invasion/migration, such as adhesion[122] and cell-cell interactions[123,124], could be used to identify synergistic treatments. Future work will define the extent to which HTF may identify novel hits in the HT screening space relative to existing methods.

Conclusion

Here we describe the HTF method, which provides a scalable platform for simultaneous measurements of cell filtration. We show that HTF captures differences in the filtration of different cell types, including malignant versus benign, cisplatin-resistant versus cisplatin-sensitive cells, epithelial-type versus mesenchymal-type cells, as well as the effects of small molecules that alter the cytoskeleton and nucleus. As HTF evaluates the ability of single cells to passively deform through narrow gaps on the timescale of seconds to minutes, the method offers unique advantages that complement existing cell invasion assays which measure the ability of cells to actively migrate through narrow geometries[125-127]. Importantly, HTF bridges the gap in throughput between measurements of cell deformability and HT screening, which opens up opportunities to uncover novel molecules or pathways that regulate cell deformability. While we have demonstrated here the application of cell filtration to screen cancer cells, changes in cell physical properties are implicated in a range of diseases from blood disorders[128] to neurodegenerative diseases such as Alzheimer's[129]. Cell filtration thus has potential to be used as a scalable readout for drug discovery in diverse disease contexts.

Author contributions

ACR, DQ and NKG invented the technology and designed the experiments. NKG performed all experiments. CL contributed to experiments and data collection. KDN conducted simulations. LL, DQ, BT, and RD contributed to design of the device and experimental setup. OD, JR, RW, BK, KL, MRS and MRF contributed cells and biological insight. NKG and ACR wrote the manuscript. All authors reviewed the manuscript.

Acknowledgements

We are grateful to the National Science Foundation (CAREER DBI-1254185 to ACR), the Department of Defense (Ovarian Cancer Research Fund Pilot Award), and the Farber Family Foundation.

Competing financial interests

The authors declare no competing financial interest.

References

1. W. F. An and N. Tolliday, *Mol Biotechnol*, 2010, **45**, 180-186.

2. J. T. Fox and K. Myung, *Oncotarget*, 2012, **3**, 581-585.

3. P. Szymanski, M. Markowicz and E. Mikiciuk-Olasik, *Int J Mol Sci*, 2012, **13**, 427-452.

4. G. S. Du, J. Z. Pan, S. P. Zhao, Y. Zhu, J. M. den Toonder and Q. Fang, *Anal Chem*, 2013, **85**, 6740-6747.

5. K. Guo, A. A. Shelat, R. K. Guy and M. B. Kastan, *J Biomol Screen*, 2014, **19**, 538-546.

6. T. Miyagi, B. Shiotani, R. Miyoshi, T. Yamamoto, T. Oka, K. Umezawa, T. Ochiya, M. Takano and H. Tahara, *Cancer Sci*, 2014, **105**, 870-874.

7. A. M. Baker, W. Huang, X. M. Wang, M. Jansen, X. J. Ma, J. Kim, C. M. Anderson, X. Wu, L. Pan, N. Su, Y. Luo, E. Domingo, T. Heide, A. Sottoriva, A. Lewis, A. D. Beggs, N. A. Wright, M. Rodriguez-Justo, E. Park, I. Tomlinson and T. A. Graham, *Nat Commun*, 2017, **8**, 1998.

8. H. L. Martin, M. Adams, J. Higgins, J. Bond, E. E. Morrison, S. M. Bell, S. Warriner, A. Nelson and D. C. Tomlinson, *PLoS One*, 2014, **9**, e88338.

9. A. H. Wong, H. Li, Y. Jia, P. I. Mak, R. Martins, Y. Liu, C. M. Vong, H. C. Wong, P. K. Wong, H. Wang, H. Sun and C. X. Deng, *Sci Rep*, 2017, **7**, 9109.

10. L. Zhang, Z. Yang, L. Granieri, A. Pasculescu, A. Datti, S. L. Asa, Z. Xu and S. Ezzat, *Oncotarget*, 2016, **7**, 19948-19959.

11. O. S. Frankfurt and A. Krishan, *Anticancer Drugs*, 2003, **14**, 555-561.

12. N. A. Evensen, J. Li, J. Yang, X. Yu, N. S. Sampson, S. Zucker and J. Cao, *PLoS One*, 2013, **8**, e82811.

13. H. A. Kenny, M. Lal-Nag, E. A. White, M. Shen, C. Y. Chiang, A. K. Mitra, Y. Zhang, M. Curtis, E. M. Schryver, S. Bettis, A. Jadhav, M. B. Boxer, Z. Li, M. Ferrer and E. Lengyel, *Nat Commun*, 2015, **6**, 6220.

14. G. Cassinelli, *Tumori*, 2016, **2016**, 226-235.

15. G. W. Aherne, E. McDonald and P. Workman, *Breast Cancer Res*, 2002, **4**, 148-154.

16. R. C. Donehower, *Stem Cells*, 1996, **14**, 25-28.

17. J. K. Chan, M. K. Cheung, A. Husain, N. N. Teng, D. West, A. S. Whittemore, J. S. Berek and K. Osann, *Obstet Gynecol*, 2006, **108**, 521-528.

18. J. D. Wright, L. Chen, A. I. Tergas, S. Patankar, W. M. Burke, J. Y. Hou, A. I. Neugut, C. V. Ananth and D. L. Hershman, *Obstet Gynecol*, 2015, **125**, 1345-1352.

19. T. Shimada, T. Saito, M. Shimokawa, K. Shimamoto, S. Matsushita, S. Yamaguchi, K. Ariyoshi and M. Okadome, *Jpn J Clin Oncol*, 2017, **47**, 494-498.

20. A. Kim, Y. Ueda, T. Naka and T. Enomoto, *J Exp Clin Cancer Res*, 2012, **31**, 14.

21. J. Y. Lee, S. Kim, Y. T. Kim, M. C. Lim, B. Lee, K. W. Jung, J. W. Kim, S. Y. Park and Y. J. Won, *BMC Cancer*, 2018, **18**, 601.

22. C. N. Qian, Y. Mei and J. Zhang, *Chin J Cancer*, 2017, **36**, 38.

23. H. Zahreddine and K. L. Borden, *Front Pharmacol*, 2013, **4**, 28.

24. T. R. Wilson, P. G. Johnston and D. B. Longley, *Curr Cancer Drug Targets*, 2009, **9**, 307-319.

25. D. Wirtz, K. Konstantopoulos and P. C. Searson, *Nat Rev Cancer*, 2011, **11**, 512-522.

26. S. M. Fendt, *Front Endocrinol (Lausanne)*, 2017, **8**, 150.

27. A. Fuhrmann, A. Banisadr, P. Beri, T. D. Tlsty and A. J. Engler, *Biophys J*, 2017, **112**, 736-745.

28. D. Qi, N. Kaur Gill, C. Santiskulvong, J. Sifuentes, O. Dorigo, J. Rao, B. Taylor-Harding, W. Ruprecht Wiedemeyer and A. C. Rowat, *Sci Rep*, 2015, **5**, 17595.

29. K. D. Nyberg, S. L. Bruce, A. V. Nguyen, C. K. Chan, N. K. Gill, T. H. Kim, E. K. Sloan and A. C. Rowat, *Integr Biol (Camb)*, 2018, **10**, 218-231.

30. J. Hamann and M. Overholtzer, *Cell Res*, 2016, **26**, 637-638.

31. H. T. Tse, D. R. Gossett, Y. S. Moon, M. Masaeli, M. Sohsman, Y. Ying, K. Mislick, R. P. Adams, J. Rao and D. Di Carlo, *Sci Transl Med*, 2013, **5**, 212ra163.

32. W. A. Lam, M. J. Rosenbluth and D. A. Fletcher, *Blood*, 2007, **109**, 3505-3508.

33. S. E. Cross, Y. S. Jin, Q. Y. Lu, J. Rao and J. K. Gimzewski, *Nanotechnology*, 2011, **22**, 215101.

34. A. El Kaffas, D. Bekah, M. Rui, J. C. Kumaradas and M. C. Kolios, *Phys Med Biol*, 2013, **58**, 923-936.

35. M. A. Tsai, R. E. Waugh and P. C. Keng, *Biophys J*, 1998, **74**, 3282-3291.

36. S. Sharma, C. Santiskulvong, J. Rao, J. K. Gimzewski and O. Dorigo, *Integr Biol (Camb)*, 2014, **6**, 611-617.

37. M. Morgan-Fisher, U. M. Wewer and A. Yoneda, *J Histochem Cytochem*, 2013, **61**, 185-198.

38. A. Surcel, W. P. Ng, H. West-Foyle, Q. Zhu, Y. Ren, L. B. Avery, A. K. Krenc, D. J. Meyers, R. S. Rock, R. A. Anders, C. L. Freel Meyers and D. N. Robinson, *Proc Natl Acad Sci U S A*, 2015, **112**, 1428-1433.

39. A. Gandalovicova, D. Rosel, M. Fernandes, P. Vesely, P. Heneberg, V. Cermak, L. Petruzelka, S. Kumar, V. Sanz-Moreno and J. Brabek, *Trends Cancer*, 2017, **3**, 391-406.

40. W. Xu, R. Mezencev, B. Kim, L. Wang, J. McDonald and T. Sulchek, *PLoS One*, 2012, **7**, e46609.

41. T. H. Kim, N. K. Gill, K. D. Nyberg, A. V. Nguyen, S. V. Hohlbauch, N. A. Geisse, C. J. Nowell, E. K. Sloan and A. C. Rowat, *J Cell Sci*, 2016, **129**, 4563-4575.

42. A. V. Nguyen, K. D. Nyberg, M. B. Scott, A. M. Welsh, A. H. Nguyen, N. Wu, S. V. Hohlbauch, N. A. Geisse, E. A. Gibb, A. G. Robertson, T. R. Donahue and A. C. Rowat, *Integr Biol (Camb)*, 2016, **8**, 1232-1245.

43. S. V. Nemtsev, O. Zueva, M. R. Khismatullin, A. I. Al'bulov and V. P. Varlamov, *Prikl Biokhim Mikrobiol*, 2004, **40**, 46-50.

44. H. Son and A. Moon, *Toxicol Res*, 2010, **26**, 245-252.

45. R. M. Hochmuth and D. Needham, *Biorheology*, 1990, **27**, 817-828.

46. O. Thoumine and A. Ott, *J Cell Sci*, 1997, **110 (Pt 17)**, 2109-2116.

47. S. E. Cross, Y. S. Jin, J. Rao and J. K. Gimzewski, *Nat Nanotechnol*, 2007, **2**, 780-783.

48. M. J. Rosenbluth, W. A. Lam and D. A. Fletcher, *Biophys J*, 2006, **90**, 2994-3003.

49. O. Otto, P. Rosendahl, A. Mietke, S. Golfier, C. Herold, D. Klaue, S. Girardo, S. Pagliara, A. Ekpenyong, A. Jacobi, M. Wobus, N. Topfner, U. F. Keyser, J. Mansfeld, E. Fischer-Friedrich and J. Guck, *Nat Methods*, 2015, **12**, 199-202, 194 p following 202.

50. A. Adamo, A. Sharei, L. Adamo, B. Lee, S. Mao and K. F. Jensen, *Anal Chem*, 2012, **84**, 6438-6443.

51. D. R. Gossett, H. T. Tse, S. A. Lee, Y. Ying, A. G. Lindgren, O. O. Yang, J. Rao, A. T. Clark and D. Di Carlo, *Proc Natl Acad Sci U S A*, 2012, **109**, 7630-7635.

52. N. K. Gill, D. Qi, T.-H. Kim, C. Chan, A. Nguyen, K. D. Nyberg and A. C. Rowat, 2017.

53. O. K. Baskurt, D. Gelmont and H. J. Meiselman, *Am J Respir Crit Care Med*, 1998, **157**, 421-427.

54. Y. Kikuchi, T. Arai and T. Koyama, *Med Biol Eng Comput*, 1983, **21**, 270-276.

55. H. L. Reid, A. J. Barnes, P. J. Lock, J. A. Dormandy and T. L. Dormandy, *J Clin Pathol*, 1976, **29**, 855-858.

56. J. S. Marcus, W. F. Anderson and S. R. Quake, *Anal Chem*, 2006, **78**, 956-958.

57. M. Muluneh and D. Issadore, *Lab Chip*, 2013, **13**, 4750-4754.

58. W. Y. Ma, L. C. Hsiung, C. H. Wang, C. L. Chiang, C. H. Lin, C. S. Huang and A. M. Wo, *Sci Rep*, 2015, **5**, 9656.

59. G. Du, Q. Fang and J. M. den Toonder, *Anal Chim Acta*, 2016, **903**, 36-50.

60. S. Vyawahare, A. D. Griffiths and C. A. Merten, *Chem Biol*, 2010, **17**, 1052-1065.

61. K. D. Nyberg, K. H. Hu, S. H. Kleinman, D. B. Khismatullin, M. J. Butte and A. C. Rowat, *Biophys J*, 2017, **113**, 1574-1584.

62. Y. J. Fu, H. Z. Qui, K. S. Liao, S. J. Lue, C. C. Hu, K. R. Lee and J. Y. Lai, *Langmuir*, 2010, **26**, 4392-4399.

63. K. D. Nyberg, M. B. Scott, S. L. Bruce, A. B. Gopinath, D. Bikos, T. G. Mason, J. W. Kim, H. S. Choi and A. C. Rowat, *Lab Chip*, 2016, **16**, 3330-3339.

64. R. S. Frank and M. A. Tsai, *J Biomech Eng*, 1990, **112**, 277-282.

65. S. Byun, S. Son, D. Amodei, N. Cermak, J. Shaw, J. H. Kang, V. C. Hecht, M. M. Winslow, T. Jacks, P. Mallick and S. R. Manalis, *Proc Natl Acad Sci U S A*, 2013, **110**, 7580-7585.

66. M. J. Rosenbluth, W. A. Lam and D. A. Fletcher, *Lab Chip*, 2008, **8**, 1062-1070.

67. D. J. Hoelzle, B. A. Varghese, C. K. Chan and A. C. Rowat, *J Vis Exp*, 2014, DOI: 10.3791/51474, e51474.

68. A. C. Rowat, D. E. Jaalouk, M. Zwerger, W. L. Ung, I. A. Eydelnant, D. E. Olins, A. L. Olins, H. Herrmann, D. A. Weitz and J. Lammerding, *J Biol Chem*, 2013, **288**, 8610-8618.

69. S. Gabriele, A. M. Benoliel, P. Bongrand and O. Theodoly, *Biophys J*, 2009, **96**, 4308-4318.

70. K. W. Oh, K. Lee, B. Ahn and E. P. Furlani, *Lab Chip*, 2012, **12**, 515-545.

71. D. C. Duffy, J. C. McDonald, O. J. Schueller and G. M. Whitesides, *Anal Chem*, 1998, **70**, 4974-4984.

72. B. M. Jun, F. Serra, Y. Xia, H. S. Kang and S. Yang, *ACS Appl Mater Interfaces*, 2016, **8**, 30671-30676.

73. P. Kunda, A. E. Pelling, T. Liu and B. Baum, *Curr Biol*, 2008, **18**, 91-101.

74. J. Shaw Bagnall, S. Byun, S. Begum, D. T. Miyamoto, V. C. Hecht, S. Maheswaran, S. L. Stott, M. Toner, R. O. Hynes and S. R. Manalis, *Sci Rep*, 2015, **5**, 18542.

75. K. J. Chavez, S. V. Garimella and S. Lipkowitz, *Breast Dis*, 2010, **32**, 35-48.

76. H. Babahosseini, J. S. Strobl and M. Agah, *Nanotechnology*, 2015, **26**, 354004.

77. V. Swaminathan, K. Mythreye, E. T. O'Brien, A. Berchuck, G. C. Blobe and R. Superfine, *Cancer Res*, 2011, **71**, 5075-5080.

78. M. Reis-Sobreiro, J. Chen, T. Novitskaya, S. You, S. Morley, K. Steadman, N. Kaur Gill, A. Eskaros, M. Rotinen, C. Chu, L. Chung, H. Tanaka, W. Yang, B. Knudsen, H. Tseng, A. Rowat, E. Posadas, A. Zijlstra, D. Di Vizio and M. Freeman, *Cancer Res*, 2018, DOI: 10.1158/0008-5472.CAN-18-0608.

79. A. C. Rowat, J. Lammerding and J. H. Ipsen, *Biophys J*, 2006, **91**, 4649-4664.

80. J. Lammerding, J. Hsiao, P. C. Schulze, S. Kozlov, C. L. Stewart and R. T. Lee, *J Cell Biol*, 2005, **170**, 781-791.

81. M. Reis-Sobreiro, J. F. Chen, T. Novitskaya, S. You, S. Morley, K. Steadman, N. Kaur Gill, A. Eskaros, M. Rotinen, C. Y. Chu, L. W. K. Chung, H. Tanaka, W. Yang, B. S. Knudsen, H. R. Tseng, A. C. Rowat, E. M. Posadas, A. Zijlstra, D. Di Vizio and M. R. Freeman, *Cancer Res*, 2018, DOI: 10.1158/0008-5472.CAN-18-0608.

82. K. Nyberg, K. Hu, S. Kleinman, D. Khismatullin, M. Butte and A. Rowat, *Biophys J*, 2017, **113**, 1574-1584.

83. J. R. Lange, J. Steinwachs, T. Kolb, L. A. Lautscham, I. Harder, G. Whyte and B. Fabry, *Biophys J*, 2015, **109**, 26-34.

84. S. Dupont, L. Morsut, M. Aragona, E. Enzo, S. Giulitti, M. Cordenonsi, F. Zanconato, J. Le Digabel, M. Forcato, S. Bicciato, N. Elvassore and S. Piccolo, *Nature*, 2011, **474**, 179-183.

85. B. Zhao, X. Ye, J. Yu, L. Li, W. Li, S. Li, J. Yu, J. D. Lin, C. Y. Wang, A. M. Chinnaiyan, Z. C. Lai and K. L. Guan, *Genes Dev*, 2008, **22**, 1962-1971.

86. K. J. Chalut, M. Hopfler, F. Lautenschlager, L. Boyde, C. J. Chan, A. Ekpenyong, A. Martinez-Arias and J. Guck, *Biophys J*, 2012, **103**, 2060-2070.

87. S. Graff-Iversen, S. A. Anderssen, I. M. Holme, A. K. Jenum and T. Raastad, *Eur J Epidemiol*, 2008, **23**, 167-174.

88. D. W. Goddette and C. Frieden, *J Biol Chem*, 1986, **261**, 15974-15980.

89. M. A. Tsai, R. S. Frank and R. E. Waugh, *Biophys J*, 1994, **66**, 2166-2172.

90. T. Wakatsuki, B. Schwab, N. C. Thompson and E. L. Elson, *J Cell Sci*, 2001, **114**, 1025-1036.

91. H. I. Jung, I. Shin, Y. M. Park, K. W. Kang and K. S. Ha, *Mol Cells*, 1997, **7**, 431-437.

92. S. Chien and K. L. Sung, *Biophys J*, 1984, **46**, 383-386.

93. I. Arnal and R. H. Wade, *Curr Biol*, 1995, **5**, 900-908.

94. C. J. Chan, A. E. Ekpenyong, S. Golfier, W. Li, K. J. Chalut, O. Otto, J. Elgeti, J. Guck and F. Lautenschlager, *Biophys J*, 2015, **108**, 1856-1869.

95. A. X. Cartagena-Rivera, J. S. Logue, C. M. Waterman and R. S. Chadwick, *Biophys J*, 2016, **110**, 2528-2539.

96. J. C. Martens and M. Radmacher, *Pflugers Arch*, 2008, **456**, 95-100.

97. L. Haviv, D. Gillo, F. Backouche and A. Bernheim-Groswasser, *J Mol Biol*, 2008, **375**, 325-330.

98. S. Boland, E. Boisvieux-Ulrich, O. Houcine, A. Baeza-Squiban, M. Pouchelet, D. Schoevaert and F. Marano, *J Cell Sci*, 1996, **109 (Pt 9)**, 2207-2219.

99. S. Edlund, M. Landstrom, C. H. Heldin and P. Aspenstrom, *Mol Biol Cell*, 2002, **13**, 902-914.

100. Y. Qiao, J. Chen, Y. B. Lim, M. L. Finch-Edmondson, V. P. Seshachalam, L. Qin, T. Jiang, B. C. Low, H. Singh, C. T. Lim and M. Sudol, *Cell Rep*, 2017, **19**, 1495-1502.

101. G. Nardone, J. Oliver-De La Cruz, J. Vrbsky, C. Martini, J. Pribyl, P. Skladal, M. Pesl, G. Caluori, S. Pagliari, F. Martino, Z. Maceckova, M. Hajduch, A. Sanz-Garcia, N. M. Pugno, G. B. Stokin and G. Forte, *Nat Commun*, 2017, **8**, 15321.

102. R. J. Pelham, Jr. and Y. Wang, *Proc Natl Acad Sci U S A*, 1997, **94**, 13661-13665.

103. J. L. Leight, M. A. Wozniak, S. Chen, M. L. Lynch and C. S. Chen, *Mol Biol Cell*, 2012, **23**, 781-791.

104. J. W. O'Connor and E. W. Gomez, *Clin Transl Med*, 2014, **3**, 23.

105. A. Kulkarni, A. Chatterjee, P. Kondaiah and N. Gundiah, *Phys Biol*, 2018, DOI: 10.1088/1478-3975/aac3ba.

106. Q. Zheng, J. Long, B. Jia, X. Xu, C. Zhang, L. Li, Z. Wen, F. Jin, W. Yao and Z. Zeng, *Clin Hemorheol Microcirc*, 2014, **56**, 25-40.

107. H. Zhang, S. K. Ramakrishnan, D. Triner, B. Centofanti, D. Maitra, B. Gyorffy, J. S. Sebolt-Leopold, M. K. Dame, J. Varani, D. E. Brenner, E. R. Fearon, M. B. Omary and Y. M. Shah, *Sci Signal*, 2015, **8**, ra98.

108. F. Gibault, M. Corvaisier, F. Bailly, G. Huet, P. Melnyk and P. Cotelle, *Curr Med Chem*, 2016, **23**, 1171-1184.

109. A. C. Rowat, J. Lammerding, H. Herrmann and U. Aebi, *Bioessays*, 2008, **30**, 226-236.

110. K. Wolf, M. Te Lindert, M. Krause, S. Alexander, J. Te Riet, A. L. Willis, R. M. Hoffman, C. G. Figdor, S. J. Weiss and P. Friedl, *J Cell Biol*, 2013, **201**, 1069-1084.

111. K. F. Toth, T. A. Knoch, M. Wachsmuth, M. Frank-Stohr, M. Stohr, C. P. Bacher, G. Muller and K. Rippe, *J Cell Sci*, 2004, **117**, 4277-4287.

112. G. Galiova, E. Bartova, I. Raska, J. Krejci and S. Kozubek, *Eur J Cell Biol*, 2008, **87**, 291-303.

113. J. H. Zhang, T. D. Chung and K. R. Oldenburg, *J Biomol Screen*, 1999, **4**, 67-73.

114. U. N. Lee, X. Su, D. J. Guckenberger, A. M. Dostie, T. Zhang, E. Berthier and A. B. Theberge, *Lab Chip*, 2018, **18**, 496-504.

115. C. Iliescu, H. Taylor, M. Avram, J. Miao and S. Franssila, *Biomicrofluidics*, 2012, **6**, 16505-1650516.

116. S. M. Thomas and J. R. Grandis, *Cell Cycle*, 2011, **10**, 2626-2627.

117. M. J. Alvarez Cubero, J. A. Lorente, I. Robles-Fernandez, A. Rodriguez-Martinez, J. L. Puche and M. J. Serrano, *Methods Mol Biol*, 2017, **1634**, 283-303.

118. L. T. Li, G. Jiang, Q. Chen and J. N. Zheng, *Mol Med Rep*, 2015, **11**, 1566-1572.

119. J. Chen, W. Zhou, Q. Jia, J. Chen, S. Zhang, W. Yao, F. Wei, Y. Zhang, F. Yang, W. Huang, Y. Zhang, H. Zhang, Y. Zhang, B. Huang, Z. Zhang, H. Jia and N. Wang, *Sci Rep*, 2016, **6**, 19304.

120. S. P. Carey, T. M. D'Alfonso, S. J. Shin and C. A. Reinhart-King, *Crit Rev Oncol Hematol*, 2012, **83**, 170-183.

121. M. L. Circu, S. S. Dykes, J. Carroll, K. Kelly, F. Galiano, A. Greer, J. Cardelli and H. El-Osta, *PLoS One*, 2016, **11**, e0146931.

122. H. A. Kenny, M. Lal-Nag, E. A. White, M. Shen, C. Y. Chiang, A. K. Mitra, Y. Zhang, M. Curtis, E. M. Schryver, S. Bettis, A. Jadhav, M. B. Boxer, Z. Li, M. Ferrer and E. Lengyel, *Nat Commun*, 2016, **7**, 10649.

123. I. Y. Wong, S. Javaid, E. A. Wong, S. Perk, D. A. Haber, M. Toner and D. Irimia, *Nat Mater*, 2014, **13**, 1063-1071.

124. S. H. Au, B. D. Storey, J. C. Moore, Q. Tang, Y. L. Chen, S. Javaid, A. F. Sarioglu, R. Sullivan, M. W. Madden, R. O'Keefe, D. A. Haber, S. Maheswaran, D. M. Langenau, S. L. Stott and M. Toner, *Proc Natl Acad Sci U S A*, 2016, **113**, 4947-4952.

125. Y. C. Chen, B. Humphries, R. Brien, A. E. Gibbons, Y. T. Chen, T. Qyli, H. R. Haley, M. E. Pirone, B. Chiang, A. Xiao, Y. H. Cheng, Y. Luan, Z. Zhang, J. Cong, K. E. Luker, G. D. Luker and E. Yoon, *Sci Rep*, 2018, **8**, 244.

126. L. A. Lautscham, C. Kammerer, J. R. Lange, T. Kolb, C. Mark, A. Schilling, P. L. Strissel, R. Strick, C. Gluth, A. C. Rowat, C. Metzner and B. Fabry, *Biophys J*, 2015, **109**, 900-913.

127. C. M. Denais, R. M. Gilbert, P. Isermann, A. L. McGregor, M. te Lindert, B. Weigelin, P. M. Davidson, P. Friedl, K. Wolf and J. Lammerding, *Science*, 2016, **352**, 353-358.

128. G. Tomaiuolo, *Biomicrofluidics*, 2014, **8**, 051501.

129. A. A. Ungureanu, I. Benilova, O. Krylychkina, D. Braeken, B. De Strooper, C. Van Haesendonck, C. G. Dotti and C. Bartic, *Sci Rep*, 2016, **6**, 25841.